7
Diffraction at high energy

The observables discussed in this book so far have been limited to total cross sections and the related structure functions. To calculate these quantities one does not need to impose any constraints on the final state. We now present a small-x calculation of a more exclusive quantity, the cross section for diffractive dissociation, where one requires that the final state has at least one rapidity gap, i.e., a region of rapidity where no particles are produced. We again tackle the problem using the two-step formalism of Chapters 4 and 5: we first calculate the cross sections for quasi-elastic processes using the classical MV/GGM approximation and then include small-x evolution corrections in the resulting expression. For diffractive dissociation where the produced hadrons have large invariant mass, we develop a nonlinear evolution equation that describes the process.

7.1 General concepts

7.1.1 Diffraction in optics

Diffraction is a typical process in which we can see the wave nature of particles. When thinking of diffraction one usually pictures the diffraction of light, when a plane wave is incident on an aperture or an obstacle (see Fig. 7.1) and forms a diffraction pattern on the screen behind. The diffraction pattern consists of a bright spot in the middle and a series of maxima and minima of light intensity around it, as shown schematically in Fig. 7.1. The positions of these maxima and minima depend on the size R of the obstacle or aperture (the target), the distance d between the target and the screen (the detector), and the light wavelength λ. Depending on the values of these three parameters one usually distinguishes three types of diffraction, as follows.

(i) Fraunhofer diffraction, when $R^2/(\lambda\, d) \ll 1$, which corresponds to the scattering at very small angles;
(ii) Fresnel diffraction, when $R^2/(\lambda\, d) \approx 1$, which corresponds to the scattering at small (but not very small) angles;
(iii) geometrical optics, when $R^2/(\lambda\, d) \gg 1$ and we recover the light-ray picture.

Keeping λ and R fixed, one can see that when the screen is close to the obstacle or aperture (i.e., at small d) we have geometrical optics. As we move the screen further away from the

https://doi.org/10.1017/9781009291446.008 Published online by Cambridge University Press

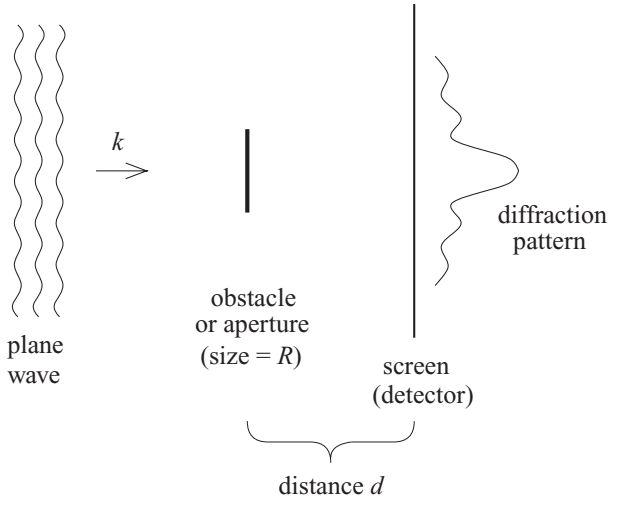

Fig. 7.1. The diffraction pattern for the scattering of light.

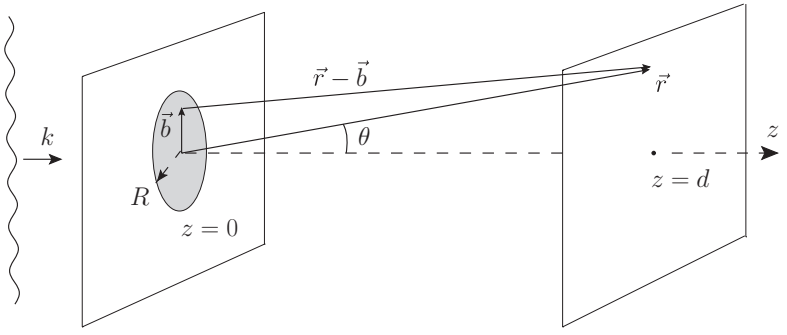

Fig. 7.2. The diffraction of a plane wave with momentum (wave vector) k by a circular aperture of radius R in a plane screen at $z = 0$. We observe the diffraction pattern on another plane screen at $z = d$.

target we go through a region of Fresnel diffraction, and, far away from the target, we enter the region of Fraunhofer diffraction. As our goal here is to build an optical analogy to the high energy scattering of particles, when the detector is far from the target (compared with the particle size and wavelength), we see that we need to study Fraunhofer diffraction.

To be more specific, consider diffraction on a circular aperture in an infinite plane screen, with the detector also an infinite plane screen, as shown in Fig. 7.2. We are interested in the shape of the diffraction pattern on the screen. Our calculation is going to be rather brief, as we assume that the reader is familiar with the theory of diffraction in optics. For a more detailed theoretical discussion of the diffraction of light we refer the reader to the book of Jackson (1998) (Sections 10.5–10.11). For simplicity we also imagine that instead of electromagnetic light we have some massless scalar field $\phi(t, \vec{r})$. The plane

https://doi.org/10.1017/9781009291446.008 Published online by Cambridge University Press

wave is incident along the z-axis and is described by $\phi_{inc}(t,\vec{r}) = e^{-i\omega t+ikz}\phi_0$, where ω is the frequency and $k = 2\pi/\lambda$ is the wave number. According to the Huygens–Fresnel principle, the field at the detector screen located at $z = d$, is given by the sum of the spherical waves $\exp(ik|\vec{r}-\vec{b}|)/(4\pi|\vec{r}-\vec{b}|)$ coming from every point in the aperture. Here $\vec{r}-\vec{b}$ is the distance vector connecting point $\vec{b}$ in the aperture and point $\vec{r}$ on the screen (see Fig. 7.2). For $d \gg \lambda$ the field at the screen (the scattered field) can be written in terms of a generalized Kirchhoff integral as

$$\phi_{sc}(\vec{r}\,) = \frac{k}{2\pi i}\int\limits_{\text{aperture}} d^2b_\perp \frac{e^{ik|\vec{r}-\vec{b}|}}{|\vec{r}-\vec{b}|}\frac{(\vec{r}-\vec{b})_z}{|\vec{r}-\vec{b}|}\,\phi_{inc}\left(\vec{b}_\perp, z=0\right), \tag{7.1}$$

where the integral is over the two-dimensional surface of the aperture located at $z = 0$ and $\phi_{sc}(t,\vec{r}) = e^{-i\omega t}\phi_{sc}(\vec{r})$.

For Fraunhofer diffraction we can expand the exponent of Eq. (7.1) to give $|\vec{r}-\vec{b}| = r - b\sin\theta + O(b^2/r)$, where θ is the angle between $\vec{r}$ and the z-axis, $r = |\vec{r}|$, and $b = |\vec{b}|$. Using this expansion along with $(\vec{r}-\vec{b})_z/|\vec{r}-\vec{b}| \approx 1$ we can rewrite the Kirchhoff integral of Eq. (7.1) in the form

$$\begin{aligned}\phi_{sc}(\vec{r}) &= \frac{k}{2\pi i}\frac{e^{ikr}}{r}\int\limits_{\text{aperture}} d^2b_\perp e^{-ikb\sin\theta}\phi_0 \\ &= \frac{k}{2\pi i}\frac{e^{ikr}}{r}\int\limits_{\text{aperture}} d^2b_\perp e^{-i\vec{q}\cdot\vec{b}}\phi_0 = \frac{e^{ikr}}{r}f(\vec{q}\,),\end{aligned} \tag{7.2}$$

where $\vec{q} = \vec{k}' - \vec{k}$ is the recoil momentum (wave vector) and $\vec{k}'$ is the wave vector of the scattered spherical wave with magnitude equal to k and direction parallel to $\vec{r}$. Note that $\vec{b} = (\vec{b}_\perp, z = 0)$. The function $f(\vec{q})$ is defined as

$$f(\vec{q}) = \frac{k}{2\pi i}\int\limits_{\text{aperture}} d^2b_\perp e^{-i\vec{q}\cdot\vec{b}}\phi_0 \tag{7.3}$$

and corresponds to the scattering amplitude.

The (time-averaged) energy densities in the incident and scattered waves are given by

$$I_{inc} = \frac{\omega^2|\phi_{inc}|^2}{2} = \frac{\omega^2\phi_0^2}{2} \quad \text{and} \quad I_{sc} = \frac{\omega^2|\phi_{sc}|^2}{2} = \frac{\omega^2\phi_0^2}{2}\,\frac{|f(\vec{q}\,)|^2}{r^2}. \tag{7.4}$$

Defining the differential scattering cross section as the ratio of the outgoing energy in an infinitesimal solid angle $d\Omega$ and the flux of energy in the incoming wave we obtain

$$d\sigma = \frac{I_{sc}r^2 d\Omega}{I_{inc}} = |f(\vec{q})|^2 d\Omega. \tag{7.5}$$

For the circular aperture of radius R in Fig. 7.2 we have

$$f(\vec{q}) = \frac{k}{2\pi i}\int d^2b_\perp e^{-i\vec{q}\cdot\vec{b}}\,\theta(R-b) = -ik\int_0^R dbbJ_0(bq) = -i\frac{kR}{q}J_1(qR), \tag{7.6}$$

https://doi.org/10.1017/9781009291446.008 Published online by Cambridge University Press

where $q = |\vec{q}|$ and $b = |\vec{b}_\perp|$. Using this result in Eq. (7.5) and writing $d\Omega = 2\pi d\cos\theta$ with $\sin\theta \approx \theta \approx q/k$ leads to the cross section

$$\frac{d\sigma}{dt} = \pi R^2 \frac{J_1^2\left(\sqrt{|t|}R\right)}{|t|}, \tag{7.7}$$

where we have introduced the Mandelstam variable $t = -\vec{q}^{\,2}$ in direct analogy with the scattering of particles.

From Eq. (7.7) one can see that the differential cross section has a series of minima (zeroes) at $R\sqrt{|t|} = Rq = Rk\sin\theta = x_{1n}$, where x_{1n} are the zeroes of $J_1(z)$, and a series of maxima between the minima. These minima and maxima give the diffraction pattern shown in Fig. 7.1. In t-space the positions of the minima and maxima are determined solely by the target size R.

Diffraction in the context of optics, as discussed here, demonstrates that the diffraction is a direct consequence of the wave nature of light and has the characteristic structure of a differential cross section $d\sigma/dt$ as a function of t, with minima and maxima whose positions depend only on the inverse size of the target.

Certainly this introduction to the subject of light diffraction is rather short, and the analogy between optics and particle scattering is much richer and more instructive than has been demonstrated here. For the interested reader we recommend the book of Barone and Predazzi (2002), which presents the fascinating history of diffraction in optics along with discussions of optical diffraction in a framework that corresponds to particle scattering.

7.1.2 Elastic scattering and inelastic diffraction

Now we return to high energy scattering in QCD. Let us begin by considering the scattering of a projectile such as a color dipole on a nuclear target. The elastic, inelastic, and total scattering cross sections for the process can be found using Eqs. (3.119) if one knows the S-matrix for the process in impact parameter space. Equation (3.119b) can be rewritten as

$$\frac{d\sigma_{el}}{d^2b} = \left|1 - S(s,\vec{b}_\perp)\right|^2 = \left|T(s,\vec{b}_\perp)\right|^2, \tag{7.8}$$

where T is the T-matrix. Going into momentum space we obtain

$$T(s,\vec{b}_\perp) = \int \frac{d^2q}{(2\pi)^2} e^{i\vec{q}_\perp\cdot\vec{b}_\perp}\tilde{T}(s,\vec{q}_\perp) \tag{7.9}$$

and, noticing that $t = -q_\perp^2$, one can readily derive that

$$\frac{d\sigma_{el}}{dt} = \frac{1}{4\pi}\left|\tilde{T}(s,\vec{q}_\perp)\right|^2 = \frac{1}{4\pi}\left|\int d^2b e^{-i\vec{q}_\perp\cdot\vec{b}_\perp} T(s,\vec{b}_\perp)\right|^2. \tag{7.10}$$

Now consider the scattering on a target that is circular with radius R in the impact parameter plane. Moreover, assume that the black-disk limit has been reached for all impact parameters inside the target, i.e., for all $b_\perp < R$. By analogy with the dipole scattering studied earlier, we see that in this limit $T(s,\vec{b}_\perp) = iN(s,\vec{b}_\perp) = i\theta(R - b_\perp)$, where N is

https://doi.org/10.1017/9781009291446.008 Published online by Cambridge University Press

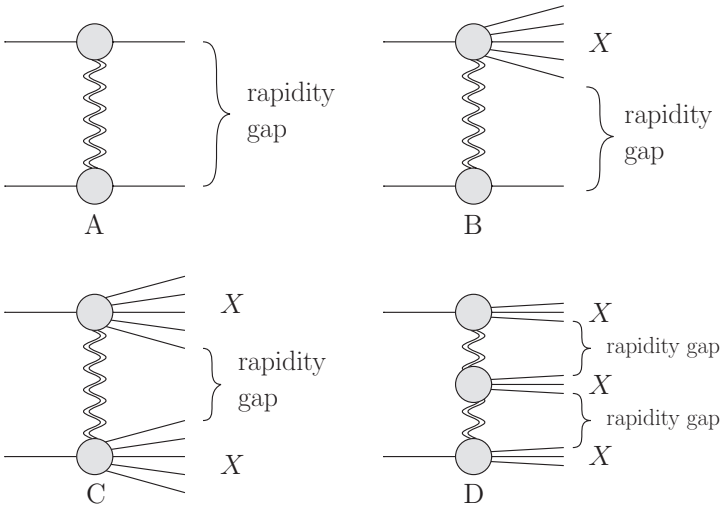

Fig. 7.3. The main types of diffraction. The double wavy lines denote pomeron exchange.

the generalization of the imaginary part of the dipole forward scattering amplitude to the case of an arbitrary projectile. Using this in Eq. (7.10) we obtain

$$\frac{d\sigma_{el}}{dt} = \pi R^2 \frac{J_1^2\left(\sqrt{|t|}R\right)}{|t|}, \tag{7.11}$$

in complete agreement with Eq. (7.7). We see that elastic scattering on a black disk in high energy physics is mathematically identical to the diffraction of light.

Indeed, in arriving at Eq. (7.7) we considered scattering on an aperture while here we have analyzed scattering on a disk, which is a different object but of a complementary shape (that is, the disk and the plane with the aperture together form a complete plane). However, Babinet's principle in optics tells us that diffraction patterns for recoil momentum $q \neq 0$ are identical for the obstacle and its complement: hence the optical diffraction pattern (7.7) is the same for a black disk of radius R, as can be verified by an explicit calculation.

The term "diffraction" in high energy scattering and the first theoretical ideas on the subject were introduced in the early 1950s by Landau, Pomeranchuk, Feinberg, Ahiezer, Ter-Mikaelyan, and Sitenko (see the review by Feinberg and Pomeranchuk (1956)). These ideas were crystallized and put into an elegant theoretical framework by Good and Walker (1960).

At high energy the term diffraction covers a much broader range than the elastic processes considered so far in this chapter. An event is considered diffractive if it contains a rapidity gap. A rapidity gap is an interval in rapidity (usually at least a few units wide) over which no particles are produced. Clearly, in elastic collisions no new particles are produced in the rapidity interval between the target and the projectile; in this case the rapidity gap covers the whole interval in rapidity.

Scattering amplitudes for the main types of diffractive event are shown in Fig. 7.3 for hadron–hadron scattering. The elastic process we have discussed above is presented

https://doi.org/10.1017/9781009291446.008 Published online by Cambridge University Press

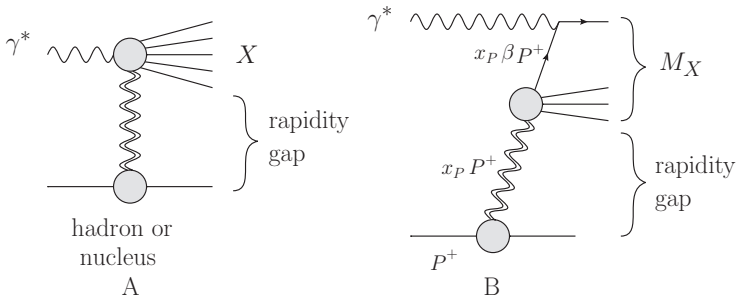

Fig. 7.4. Single diffractive dissociation in DIS: (A) a general representation of the process and (B) an explanation of the kinematic variables. The double wavy lines represent pomeron exchange, while the single wavy line denotes a virtual photon.

in panel A. The double wavy line denotes the exchange of a color-singlet object (the pomeron). Panels B through D represent various cases of inelastic diffraction, where one or both hadrons break up in the collision, that still lead to a rapidity gap or gaps. Panel B shows the process of single diffractive dissociation, where one hadron breaks up into several other hadrons denoted by X while the other stays intact. A single rapidity gap is generated in this process. One also distinguishes low- and high-mass diffraction, depending on whether the invariant mass M_X of the produced particles X is small or large. Processes with a single rapidity gap in which both hadrons dissociate, as shown in panel C of Fig. 7.3, are referred to as double diffractive dissociation. Finally, one may have more than one rapidity gap in the event: an example of a process with two rapidity gaps is shown in panel D, where hadrons are produced at mid-rapidity and are flanked by a rapidity gap on either side. Such processes are called central diffraction. If a single particle is produced at mid-rapidity then the process is referred to as central exclusive diffraction.

While diffraction in hadronic scattering represents an interesting and often challenging problem in itself, here we will concentrate on diffractive dissociation in DIS.

7.2 Diffractive dissociation in DIS

Consider single diffractive dissociation in DIS. This is a process in which a virtual photon interacts with the target, producing a number of hadrons and jets in the final state (denoted by X) but leaving the target intact and generating a rapidity gap. The process is illustrated in Fig. 7.4A. The particles X with net invariant mass M_X produced as a result of the target's breakup do not fill the whole rapidity interval; they leave a rapidity gap between the target and the "slowest" produced particle. This rapidity gap is of order $\Delta Y_{gap} = \ln[(\hat{s} + Q^2)/(M_X^2 + Q^2)]$, where $\hat{s}$ is the center-of-mass energy squared of the virtual photon–target collision (see Eq. (2.5)). (The net rapidity interval for $\hat{s} \gg Q^2$ is $Y = \ln(\hat{s}/Q^2)$, while the produced hadrons fill in the rapidity range $\Delta Y_{filled} = Y - \Delta Y_{gap} = \ln[(M_X^2 + Q^2)/Q^2]$.) No particles are produced in the rapidity gap; the existence of such a rapidity gap is indeed the characteristic signature of diffractive processes.

https://doi.org/10.1017/9781009291446.008 Published online by Cambridge University Press

Diffractive dissociation in DIS is usually described in terms of the kinematic variables x_P and β, which originate in pomeron phenomenology and are explained by Fig. 7.4B. Treating the pomeron as an effective "parton" one may describe it as carrying a fraction x_P of the incoming proton's light cone momentum. Neglecting the mass of the proton and working in the IMF with the proton moving in the light cone plus direction, we see that the pomeron will carry momentum $x_P P^\mu$, with P^μ given by Eq. (2.26) with $m = 0$. Requiring that $(x_P P + q)^2 = M_X^2$ (see Fig. 7.4B) and remembering that $\hat{s} = (P + q)^2$, we obtain

$$x_P = \frac{Q^2 + M_X^2}{Q^2 + \hat{s}}. \tag{7.12}$$

The variable β is defined as the fraction of the pomeron's light cone momentum carried by the quark that is struck by the virtual photon; thus (see Fig. 7.4B again)

$$\beta = \frac{x_{Bj}}{x_P} = \frac{Q^2}{Q^2 + M_X^2}. \tag{7.13}$$

Below we will distinguish low- and high-mass diffraction in DIS. When the invariant mass of the produced hadrons, M_X, is low, $M_X \ll Q$, which is usually the case when few hadrons are produced, we see that $\beta \approx 1$ and $x_P \approx x_{Bj}$, so that $\Delta Y_{gap} = \ln 1/x_P \approx \ln 1/x_{Bj} = Y$; the rapidity gap covers much of the net rapidity interval, as expected. When the mass M_X is large, $M_X \gg Q$, we have $\beta \ll 1$ and $x_P \approx M_X^2/\hat{s} \approx e^{-\Delta Y_{gap}}$; the rapidity gap may still be large but the rapidity interval filled by the produced hadrons is large as well.

A particularly interesting aspect of diffraction is that the typical momentum transfer appears to be of order $|t| \sim 1/R^2$, as follows from Eq. (7.11). The momentum is of order the inverse size of the target, which is in the nonperturbative QCD region (This is why t was neglected in the derivation of Eqs. (7.12) and (7.13).). It would seem, on the one hand, that diffraction is a non-perturbative process and cannot be studied within the perturbative QCD framework. On the other hand, a main postulate of the saturation or CGC approach is that saturation effects generate the saturation scale $Q_s(Y)$; this screens the IR physics, making the cross sections and other observables perturbative. On top of that, in DIS one has a hard scale Q^2, which may also be perturbatively large. We see that diffraction becomes a cross-check of the saturation approach, the main question being whether saturation physics makes diffraction a perturbative process.

7.2.1 Low-mass diffraction

To describe low-mass diffraction in DIS at high energies it is natural to start with the dipole picture of DIS presented in Sec. 4.1. Again we have a separation of scales: a virtual photon will decay into a $q\bar{q}$ pair long before hitting the target and the $q\bar{q}$ dipole interacts with the target in due course. The dipole–target interaction can be either inelastic or elastic. In Chapter 4 we showed that the total DIS cross section can be written as (see Eqs. (4.6) and (4.24))

$$\sigma_{tot}^{\gamma^* A} = \int \frac{d^2 x_\perp}{2\pi} d^2 b_\perp \int_0^1 \frac{dz}{z(1-z)} \, |\Psi^{\gamma^* \to q\bar{q}}(\vec{x}_\perp, z)|^2 \, N(\vec{x}_\perp, \vec{b}_\perp, Y). \tag{7.14}$$

https://doi.org/10.1017/9781009291446.008 Published online by Cambridge University Press

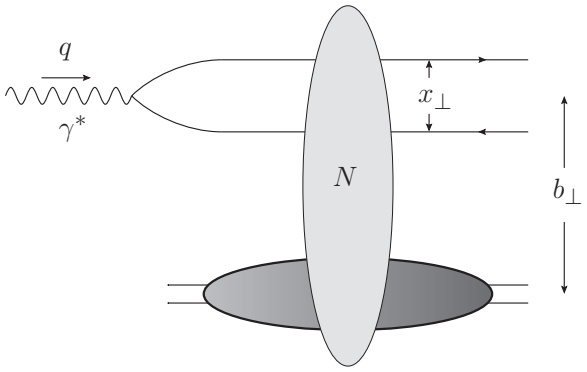

Fig. 7.5. The quasi-elastic DIS amplitude that leads to Eq. (7.17).

Omitting the part of the expression related to the virtual photon wave function, we obtain for the dipole–nucleus total cross section

$$\sigma_{tot}^{q\bar{q}A}(\vec{x}_\perp, Y) = 2\int d^2b\, N(\vec{x}_\perp, \vec{b}_\perp, Y) = 2\int d^2b \left[1 - S(\vec{x}_\perp, \vec{b}_\perp, Y)\right]. \tag{7.15}$$

We see that this is exactly Eq. (3.119a) (as S is real). By analogy with Eq. (3.119b) the elastic dipole–nucleus cross section is then

$$\sigma_{el}^{q\bar{q}A}(\vec{x}_\perp, Y) = \int d^2b \left[1 - S(\vec{x}_\perp, \vec{b}_\perp, Y)\right]^2 = \int d^2b\, N^2(\vec{x}_\perp, \vec{b}_\perp, Y). \tag{7.16}$$

The corresponding quasi-elastic DIS cross section is obtained by convoluting (7.16) with the square of the virtual photon's wave function:[1]

$$\sigma_{el}^{\gamma^* A} = \int \frac{d^2x_\perp}{4\pi} d^2b_\perp \int_0^1 \frac{dz}{z(1-z)} \left|\Psi^{\gamma^* \to q\bar{q}}(\vec{x}_\perp, z)\right|^2 N^2(\vec{x}_\perp, \vec{b}_\perp, Y). \tag{7.17}$$

Equation (7.17) was derived in the quasi-classical GGM/MV approximation, that is, with N given by Eq. (4.51), by Buchmuller, Gehrmann, and Hebecker (1997) (see also Buchmuller, McDermott, and Hebecker (1999)) and by Kovchegov and McLerran (1999). However, one can see that our derivation assumes only the decomposition of the interaction into the virtual photon's wave function and the amplitude N, with the latter independent of the light cone momentum fraction z. This assumption is also true in the LLA: hence the elastic DIS cross section (7.17) is also valid in the case when the LLA quantum evolution is included. Therefore Eq. (7.17) is true whether N is found from the BK equation (4.138) in the large-N_c limit or from the JIMWLK equation for the dipole S-matrix (5.98) when the large-N_c limit is relaxed.

The quasi-elastic DIS process corresponding to Eq. (7.17) is illustrated in Fig. 7.5. Here the virtual photon splits into a $q\bar{q}$ pair, after which the pair interacts with the target nucleus

[1] Note that the high energy $\gamma^* A$ cross section at order α_{EM} cannot be elastic, since we do not have a photon in the final state (see Fig. 7.5): we will refer to this process as quasi-elastic, to distinguish it from high-mass diffraction.

https://doi.org/10.1017/9781009291446.008 Published online by Cambridge University Press

elastically, as denoted by the oval labeled N. In the LLA approximation this means that before the interaction the dipole develops a gluon cascade, as in, say, Fig. 4.23; this cascade interacts with the target by GGM coulomb–gluon exchange and after the interaction is reabsorbed into the dipole, so that in the final state one finds only the original $q\bar{q}$ pair along with the intact nucleus. One may expect that such a process would be very rare, since it would appear highly unlikely that the gluon cascade would recombine back into the original dipole. An amazing property of elastic scattering and diffraction is that it demonstrates that such an intuition is incorrect when it comes to cross sections. Indeed, in the saturation regime, when the black-disk limit is reached and $N = 1$, we see from Eqs. (7.15) and (7.16) that

$$\frac{\sigma_{el}^{q\bar{q}A}}{\sigma_{tot}^{q\bar{q}A}} = \frac{\int d^2b N^2}{2\int d^2b N} \longrightarrow \frac{1}{2}. \tag{7.18}$$

Elastic dipole–nucleus scattering constitutes half the total cross section in very high energy collisions!

Note that in Fig. 7.5 we have two quarks in the final state: they are likely to fragment into one or several hadrons, leading to a low-M_X diffractive final state.

Using Eqs. (7.14) and Eq. (7.17) we can compare the main properties of the total and diffractive (quasi-elastic) DIS cross sections, looking for their common and different features. The large-Q^2 behavior is particularly instructive. Analyzing the virtual-photon wave functions squared in Eqs. (4.18) and (4.21) we see that, since the modified Bessel functions K_1 and K_0 fall off exponentially at large values of the argument, at large Q^2 the main contribution to the z-integral in both Eqs. (7.14) and (7.17) comes from the region $a_f x_\perp \leq 1$ with a_f given by Eq. (4.17). Neglecting for simplicity the quark masses m_f we see that this implies $\sqrt{z(1-z)} \leq 1/(Qx_\perp)$, and, since $z(1-z) < 1/4$, we either have $z \ll 1$ or $1 - z \ll 1$ if $Qx_\perp \gg 2$. Either the quark or the antiquark carries most of the virtual photon's light cone momentum. This configuration is known as the aligned-jet configuration and is the basis for the aligned-jet model (Bjorken and Kogut 1973, Nikolaev and Zakharov 1975, Frankfurt and Strikman 1988) since, in the case when the produced quark and antiquark in, say, Fig. 7.5, fragment into jets, one jet is aligned with the momentum of the virtual photon.

Concentrating on the $z \ll 1$ region (and multiplying the expression by 2 to account for the $1 - z \ll 1$ region), we can integrate over z explicitly with the help of Eqs. (4.18) and (4.21) to obtain (note that N is z-independent)

$$\begin{aligned}\int_0^1 \frac{dz}{z(1-z)} |\Psi_T^{\gamma^* \to q\bar{q}}(\vec{x}_\perp, z)|^2 &\approx 4N_c \sum_f \frac{\alpha_{EM} Z_f^2}{\pi} Q^2 \int_0^\infty dz\, z \left[K_1(x_\perp Q\sqrt{z})\right]^2 \\ &= \frac{16N_c}{3} \sum_f \frac{\alpha_{EM} Z_f^2}{\pi} \frac{1}{Q^2 x_\perp^4}\end{aligned} \tag{7.19}$$

https://doi.org/10.1017/9781009291446.008 Published online by Cambridge University Press

and

$$\int_0^1 \frac{dz}{z(1-z)} |\Psi_L^{\gamma^* \to q\bar{q}}(\vec{x}_\perp, z)|^2 \approx 16 N_c \sum_f \frac{\alpha_{EM} Z_f^2}{\pi} Q^2 \int_0^\infty dz\, z^2 \left[K_0(x_\perp Q\sqrt{z})\right]^2$$

$$= \frac{512}{15} N_c \sum_f \frac{\alpha_{EM} Z_f^2}{\pi} \frac{1}{Q^4 x_\perp^6}. \tag{7.20}$$

One can show that for $N \sim x_\perp^2$ at small $x_\perp$, which is true in the GGM (4.51) and DLA (4.150) approximations, the longitudinal contribution (7.20) is more suppressed at high Q^2 than the transverse contribution, both for $\sigma_{tot}^{\gamma^* A}$ and $\sigma_{el}^{\gamma^* A}$; therefore, we can neglect it in the large-Q^2 limit.

Noting that $Q x_\perp \gg 2$ and using Eq. (7.19) in Eqs. (7.14) and (7.17) yields, after integration over the angles of $\vec{x}_\perp$,

$$\sigma_{tot}^{\gamma^* A} \approx \frac{4 N_c \alpha_{EM}}{3\pi Q^2} \sum_f Z_f^2 \int_{4/Q^2}^\infty \frac{dx_\perp^2}{x_\perp^4} \int d^2 b_\perp 2N(x_\perp, \vec{b}_\perp, Y), \tag{7.21a}$$

$$\sigma_{el}^{\gamma^* A} \approx \frac{4 N_c \alpha_{EM}}{3\pi Q^2} \sum_f Z_f^2 \int_{4/Q^2}^\infty \frac{dx_\perp^2}{x_\perp^4} \int d^2 b_\perp N^2(x_\perp, \vec{b}_\perp, Y), \tag{7.21b}$$

where we have assumed that N is independent of the direction of $\vec{x}_\perp$.

To evaluate the integrals in Eqs. (7.21) we use the explicit leading-twist expression for the dipole amplitude N from Eq. (4.32), which is valid for $x_\perp \ll 1/Q_s$, obtaining

$$\sigma_{tot}^{\gamma^* A} \approx \frac{4\alpha_s \alpha_{EM} \pi}{3 N_c Q^2} \sum_f Z_f^2 \int_{4/Q^2}^{1/Q_s^2} \frac{dx_\perp^2}{x_\perp^2} x G_A\left(x, \frac{1}{x_\perp^2}\right), \tag{7.22a}$$

$$\sigma_{el}^{\gamma^* A} \approx \frac{\alpha_s^2 \alpha_{EM} \pi^3}{3 N_c^3 Q^2} \sum_f Z_f^2 \int_{4/Q^2}^{1/Q_s^2} dx_\perp^2 \left[x G_A\left(x, \frac{1}{x_\perp^2}\right)\right]^2, \tag{7.22b}$$

where we have used the fact that $\int d^2 b T(\vec{b}_\perp) = A$ and, in the spirit of the GGM approximation, replaced $A x G_N$ with the nuclear gluon distribution $x G_A$.

Assuming that $x G_A$ is a slowly varying function of $x_\perp$, we can see from Eqs. (7.22) that the total cross section depends on the upper limit of the $x_\perp$-integral logarithmically, while the quasi-elastic cross section depends on it quadratically. In the absence of saturation effects the integrals would have to be cut off by the nonperturbative physics in the IR, that is, we should replace Q_s by Λ_{QCD}: in such a case both cross sections would be nonperturbative, the elastic one being more so than the total. We see that saturation effects make both cross sections perturbative, even for $t = 0$ in the diffractive case, yet again justifying the perturbative QCD approximation.

https://doi.org/10.1017/9781009291446.008 Published online by Cambridge University Press

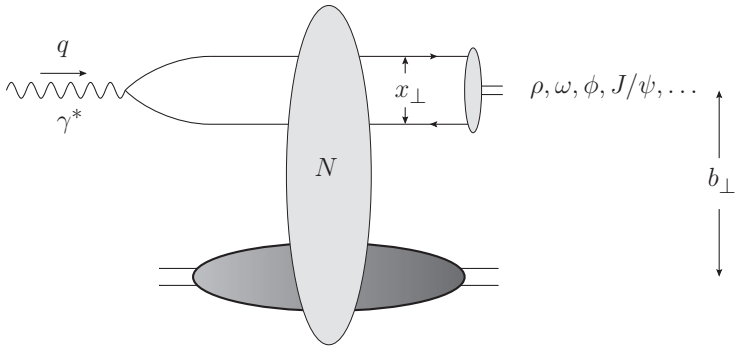

Fig. 7.6. Exclusive vector meson production amplitude in DIS.

We can make another crude approximation leading to a physical insight if we notice that in the GGM model the saturation scale squared Q_s^2 is proportional to the gluon distribution function, as follows from Eq. (4.47). Assuming that xG_A is a slowly varying function of $x_\perp$, we integrate over $x_\perp$ in Eqs. (7.22) to obtain[2]

$$\sigma_{tot}^{\gamma^* A} \propto xG_A(x, Q_s^2) \ln \frac{Q^2}{4Q_s^2}, \tag{7.23a}$$

$$\sigma_{el}^{\gamma^* A} \propto \frac{1}{Q_s^2} \left[xG_A\left(x, Q_s^2\right)\right]^2 \propto xG_A\left(x, Q_s^2\right), \tag{7.23b}$$

so that, neglecting logarithms, which are outside the precision of our approximation, the ratio $\sigma_{el}^{\gamma^* A}/\sigma_{tot}^{\gamma^* A}$ is approximately independent of Bjorken x (Kovchegov and McLerran 1999). This appears to be in approximate agreement with the data collected at HERA (see Fig. 9.2 along with Abramowicz and Dainton (1996), H1 collaboration (1997), and ZEUS collaboration (1999)).

Another important low-mass diffractive DIS process to consider is exclusive vector meson production. It is related to the quasi-elastic scattering of Eq. (7.17): in exclusive vector meson production the outgoing quark and antiquark recombine into a single vector meson. One still has a rapidity gap with the target intact in the final state. This is illustrated in Fig. 7.6. More precisely the reaction is

$$\gamma^* + p \to V\,(\rho, \omega, \phi, J/\Psi, \ldots) + p \tag{7.24}$$

for DIS on a proton; V denotes a vector meson.

The cross section of this reaction can be easily calculated using LCPT; one simply needs to find the overlap of the $q\bar{q}$ state with the (complex conjugate) light cone wave function of the vector meson Ψ^V. To see this, let us calculate the diagram in Fig. 7.6 in LCPT. The additional contributions, not present in Eq. (7.17), come from the $q\bar{q} \to V$ process: this is exactly the reverse of what is described by the vector meson's light cone wave function.

[2] Note that, while in Eq. (4.45) xG_N does not depend on x, Eq. (4.32) is still valid in the DLA region even after small-x evolution is included (cf. Eq. (4.150)), with xG depending on x.

https://doi.org/10.1017/9781009291446.008 Published online by Cambridge University Press

The cross section for exclusive vector meson production is equal to (see Ryskin (1993) for the J/Ψ production case and Brodsky *et al.* (1994) for the general case of vector meson production)

$$\sigma^{\gamma^*+A\to V+A} = \int d^2b_\perp \left| \int \frac{d^2x_\perp}{4\pi} \int_0^1 \frac{dz}{z(1-z)}\, \Psi^{\gamma^*\to q\bar{q}}(\vec{x}_\perp, z)\, N(\vec{x}_\perp, \vec{b}_\perp, Y) \Psi^V(\vec{x}_\perp, z)^* \right|^2. \quad (7.25)$$

Note that now the dipole transverse sizes in the amplitude and in the complex conjugate amplitude are different, and are integrated over separately.

In general the wave function Ψ^V is nonperturbative. In practice the main contribution of the $x_\perp$-integral in Eq. (7.25) comes from short distances, owing to the large values of Q^2 and Q_s^2 there; thus we can approximate $\Psi^V(\vec{x}_\perp, z)$ by $\Psi^V(0, z)$ (the wave function at the origin). For vector mesons $\Psi^V(0, z)$ is known from their decay into an electron–positron pair, $V \to e^+e^-$.

One can also show that the typical transverse distances in this process are of order $1/Q_s$ and so the process is, therefore, perturbative. However, the diffractive minima and maxima in the corresponding t-distribution are determined by the size of the target. To see this, we write (analogously to the transition from Eq. (7.8) to Eq. (7.10))

$$\frac{d\sigma^{\gamma^*+A\to V+A}}{dt} = \frac{1}{4\pi} \left| \int d^2b e^{-i\vec{q}_\perp\cdot\vec{b}_\perp} T^{q\bar{q}A}(\hat{s}, \vec{b}_\perp) \right|^2, \quad (7.26)$$

where now the T-matrix element is given by

$$T^{q\bar{q}A}(\hat{s}, \vec{b}_\perp) = i \int \frac{d^2x_\perp}{4\pi} \int_0^1 \frac{dz}{z(1-z)}\, \Psi^{\gamma^*\to q\bar{q}}(\vec{x}_\perp, z)\, N(\vec{x}_\perp, \vec{b}_\perp, Y) \Psi^V(\vec{x}_\perp, z)^*, \quad (7.27)$$

with $Y = \ln \hat{s}x_\perp^2$. We see that the $\vec{b}_\perp$-dependence of the T-matrix in Eq. (7.27) is given by that of N, which in turn is largely determined by the geometry of the target. Hence the positions of the diffractive maxima and minima of vector meson production are proportional to $1/R$, with R the nuclear radius. In addition, the size of the target (or, more precisely, the size of the interaction region) increases with energy; however, this increase depends mostly on nonperturbative corrections as we will discuss later.

As suggested by Munier, Stasto, and Mueller (2001), we can use Eq. (7.26) to extract the $\vec{b}_\perp$-dependence of the T-matrix (and, consequently, the S-matrix) from the experimental data, since we can invert it to write

$$T^{q\bar{q}A}(\hat{s}, \vec{b}_\perp) = \frac{i}{2\pi^{3/2}} \int d^2q e^{i\vec{q}_\perp\cdot\vec{b}_\perp} \sqrt{\frac{d\sigma^{\gamma^*+A\to V+A}}{dt}}. \quad (7.28)$$

This relation relies on the assumption that the T-matrix is purely imaginary at high energies (and hence the S-matrix is real). This assumption is certainly correct for small t, in the LLA, but at large values of t the real part of the T-matrix may not be small. In spite of this uncertainty, Eq. (7.28) shows that we can observe the T-matrix at fixed b, which, in turn,

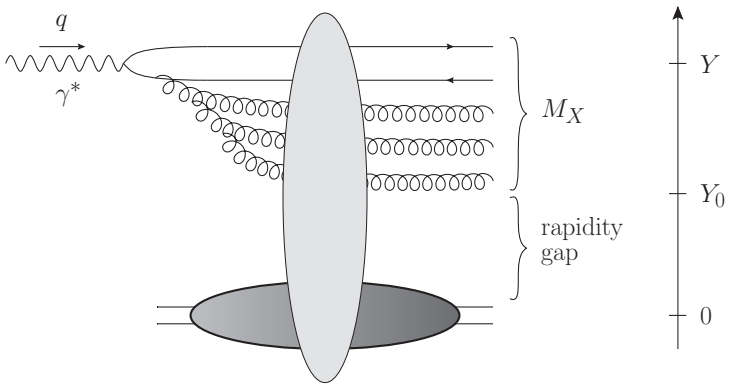

Fig. 7.7. An example of a diagram contributing to high-mass diffraction in DIS. The vertical axis on the right measures the rapidities of the particles.

can be calculated in the saturation approach. Note that the nonperturbative light cone wave function Ψ^V enters Eq. (7.27). Above we suggested a rough approximation in which the vector meson wave function was replaced by its value at the origin. For mesons consisting of heavy quarks, such as J/Ψ, or even for the Υ-meson, consisting of a $b\bar{b}$-pair, one may hope to improve on that approximation by using perturbative QCD to calculate the wave functions.

7.2.2 Nonlinear evolution equation for high-mass diffraction

So far we have considered only low-mass diffractive processes, when the gluon cascade developed by the dipole before the interaction with the nucleus is reabsorbed back into the dipole after the interaction, so that we only have the original $q\bar{q}$ dipole in the final state (along with the target), as shown in Fig. 7.5. The quark and the antiquark in the pair cannot be far from each other in rapidity, since the quark emission at small x, unlike that for gluons, is not enhanced by a logarithm of x: this is why we neglected the quark contribution to small-x evolution in the LLA. Therefore, since the invariant mass of the produced particles is related to the rapidity interval that they fill by $M_X^2 = Q^2(e^{\Delta Y_{filled}} - 1)$, we see that elastic $q\bar{q}$ pair production mainly leads to low-mass diffraction. If one wants to produce a high-mass state with a rapidity gap, one has to augment the picture of Fig. 7.5 by allowing some "fast" gluons to survive in the final state, as shown in Fig. 7.7. The process is now more complicated than that in Fig. 7.5. While the incoming dipole still develops a dipole cascade, not all the gluons in the cascade recombine back by the time the system reaches the final state: only gluons with rapidities between 0 and Y_0 recombine back, so that a rapidity gap $\Delta Y_{gap} = Y_0 - 0 = Y_0$ is formed and the target nucleus remains intact, as illustrated in Fig. 7.7. Gluons with rapidities $y > Y_0$ do not need to recombine back and thus can become "produced" gluons, as shown in Fig. 7.7. In fact some gluons with

https://doi.org/10.1017/9781009291446.008 Published online by Cambridge University Press

$y > Y_0$ may even be emitted after the GGM interaction with the target, as we will see shortly.

First let us define the observable we would like to calculate. Considering dipole–nucleus scattering, we denote by $N^D(\vec{x}_\perp, \vec{b}_\perp, Y, Y_0)$ the cross section per unit impact parameter for diffractive dissociation with a single rapidity gap stretching from 0 (the target) to some rapidity greater than or equal to Y_0. The corresponding single diffractive cross section with rapidity gap greater than or equal to Y_0 in the dipole–nucleus scattering is

$$\sigma_{diff}^{q\bar{q}A} = \int d^2b\, N^D(\vec{x}_\perp, \vec{b}_\perp, Y, Y_0). \tag{7.29}$$

If we want to find the diffraction cross section for a given fixed rapidity gap Y_0 we simply have to differentiate N^D with respect to Y_0, obtaining

$$M_X^2 \frac{d\sigma_{diff}^{q\bar{q}A}}{dM_X^2} = -\int d^2b \frac{\partial N^D(\vec{x}_\perp, \vec{b}_\perp, Y, Y_0)}{\partial Y_0}, \tag{7.30}$$

where the minus sign is due to the fact that $Y_0 = \Delta Y_{gap} \approx \ln \hat{s}/M_X^2$ for $\hat{s}$, $M_X^2 \gg Q^2$, so that $dY_0 = -dM_X^2/M_X^2$ for fixed $\hat{s}$.

By analogy with Eq. (7.17) we can use Eq. (7.29) to write down the following expression for the single diffractive cross section in DIS:

$$\sigma_{diff}^{\gamma^* A} = \int \frac{d^2x_\perp}{4\pi} d^2b_\perp \int_0^1 \frac{dz}{z(1-z)} |\Psi^{\gamma^* \to q\bar{q}}(\vec{x}_\perp, z)|^2 N^D(\vec{x}_\perp, \vec{b}_\perp, Y, Y_0). \tag{7.31}$$

The differential cross section is

$$M_X^2 \frac{d\sigma_{diff}^{\gamma^* A}}{dM_X^2} = -\int \frac{d^2x_\perp}{4\pi} d^2b_\perp \int_0^1 \frac{dz}{z(1-z)} |\Psi^{\gamma^* \to q\bar{q}}(\vec{x}_\perp, z)|^2 \frac{\partial N^D(\vec{x}_\perp, \vec{b}_\perp, Y, Y_0)}{\partial Y_0}. \tag{7.32}$$

Sometimes we will use the notation $N^D(\vec{x}_{1\perp}, \vec{x}_{0\perp}, Y, Y_0)$ for the diffractive cross section N_D of a dipole with the quark at $\vec{x}_{1\perp}$ and the antiquark at $\vec{x}_{0\perp}$; this is similar to the notation used in the forward dipole amplitude (see e.g. Eq. (4.141)).

We will assume that Y, Y_0, and $Y - Y_0$ are all large, so that $\alpha_s Y \sim 1$, $\alpha_s Y_0 \sim 1$ and $\alpha_s(Y - Y_0) \sim 1$ are all important and one has to devise a small-x resummation procedure to calculate N^D in the LLA by resumming all these parameters. We want to derive a (nonlinear) evolution equation for N^D (Kovchegov and Levin 2000). We will work in the frame where the nucleus is moving in the light cone plus direction, while the incoming dipole is moving along the minus axis. We will also employ the $A^- = 0$ light cone gauge of the (dipole) projectile.

We first observe that when $Y_0 = Y$ the rapidity gap becomes equal to the whole rapidity interval, and we have returned to the case of elastic dipole–nucleus scattering considered in Sec. 7.2.1. The elastic dipole–nucleus cross section is given in Eq. (7.16), which we can

https://doi.org/10.1017/9781009291446.008 Published online by Cambridge University Press

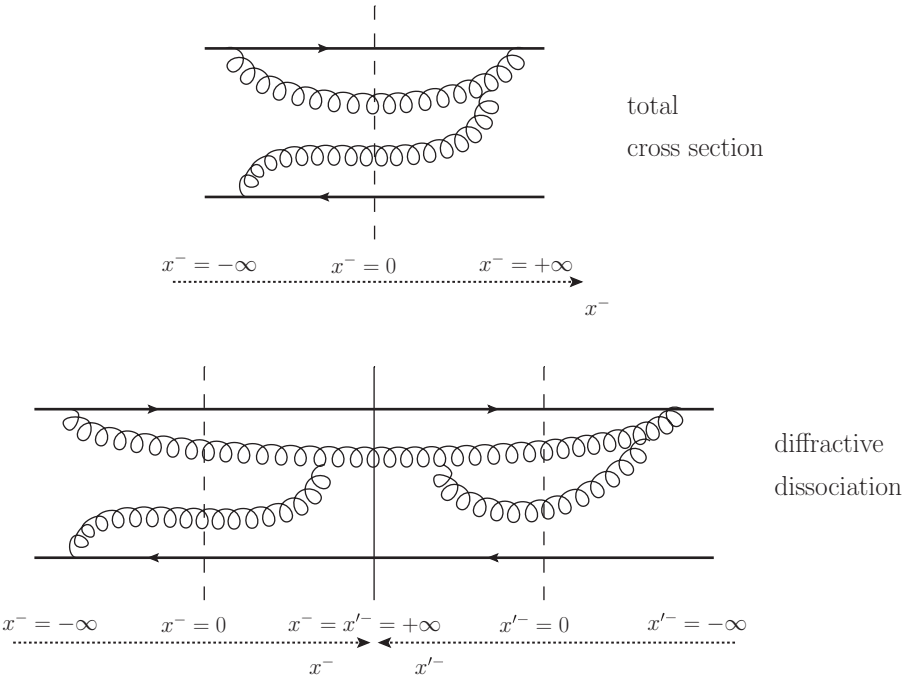

Fig. 7.8. Small-x evolution of the total cross section (upper panel) and the cross section for diffractive dissociation (lower panel).

use to write

$$N^D(\vec{x}_\perp, \vec{b}_\perp, Y = Y_0, Y_0) = N^2(\vec{x}_\perp, \vec{b}_\perp, Y_0). \tag{7.33}$$

Again in the LLA, N is given by the solution of the BK/JIMWLK equations. We will use Eq. (7.33) as the initial condition for the evolution equation that we will construct below.

From the point of view of the space–time picture, the process of diffractive production is quite different from the total cross section considered above. In calculating the total cross section we needed to find the forward scattering amplitude. For a dipole moving along the x^--axis, this means that we had to follow its evolution from $x^- = -\infty$ to the time of the GGM-type interactions at $x^- = 0$ and then again from $x^- = 0$ to the final state at $x^- = +\infty$, which, for the forward amplitude, is identical to the initial state. There are two main differences in the diffractive case (and, as we will see later, for the inclusive production cross sections as well). First, the final state at $x^- = +\infty$ is no longer identical to the initial state. Second, we cannot use the optical theorem to find the diffractive cross section: instead we have to square the scattering amplitude. This means that we have to follow the evolution of the dipole and its gluon cascade from $x^- = -\infty$ to $x^- = +\infty$ both in the amplitude and in the complex conjugate amplitude.

We illustrate the differences between the calculations of the total and diffractive cross sections in Fig. 7.8. Using the notation of Fig. 5.8 we denote by a vertical dashed line the

https://doi.org/10.1017/9781009291446.008 Published online by Cambridge University Press

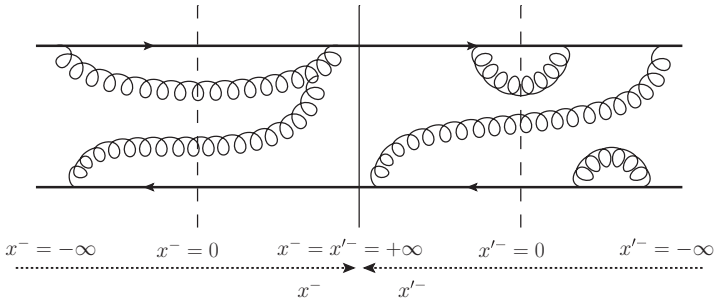

Fig. 7.9. Diagrammatic representation of the elastic scattering in Eq. (7.33).

GGM interactions with the target (along with the subsequent small-x evolution) for all the particles that cross the dashed line. The interactions with the target (and the subsequent evolution) are instantaneous compared with the lifetimes of the s-channel gluons and quarks. The forward scattering amplitude in the upper panel of Fig. 7.8 is used to obtain the total dipole–nucleus cross section. There is a single light cone time, which varies from $x^- = -\infty$ to $x^- = +\infty$, with the GGM interaction at $x^- = 0$. The lower panel shows the scattering amplitude squared: the time varies from $x^- = -\infty$ to $x^- = +\infty$ in the amplitude and in the complex conjugate amplitude (the light cone time in the latter is denoted by x'^- to distinguish it from the time in the amplitude). The vertical solid line in the lower panel of Fig. 7.8 denotes a cut; gluons may be emitted in the amplitude and then, crossing the cut, be absorbed into the complex conjugate amplitude. Such gluons exist in the final state and so are "produced". (Indeed, they fragment into hadrons in the final state: here we are using perturbative slang, in which the term "produced" implies eventual convolution with the fragmentation functions, according to the standard perturbative QCD prescription.) The gluons could be also emitted and then reabsorbed in the (complex conjugate) amplitude: such gluons are not "produced" and may contribute to the formation of the rapidity gap in which we are interested. Readers familiar with finite-temperature field theory may draw an analogy between the two light cone times x^- and x'^- and the time contour in the Schwinger–Keldysh formalism.

To illustrate further this two-time formalism we show a diagram contributing to the elastic dipole–target scattering given by Eq. (7.33) in Fig. 7.9. No gluon in Fig. 7.9 is "produced" since none crosses the cut. Instead, the evolution and the interaction with the target happen separately and independently in the amplitude and in the complex conjugate amplitude, each giving a factor N generated by the BK/JIMWLK evolution. (The interaction with the target has been assumed to be elastic in all the diagrams in this subsection; we have to use the forward, i.e., elastic dipole amplitude in the GGM approximation from Eq. (4.139) as the initial condition for the evolution for N on each side of the cut.)

An interesting question arises about the connection between the two-time amplitude-squared approach and the forward amplitude in the upper panel of Fig. 7.8. After all, we do not have to use the optical theorem to find the total cross section: we can simply square the sum of all the possible scattering amplitudes. This type of calculation would follow

https://doi.org/10.1017/9781009291446.008 Published online by Cambridge University Press

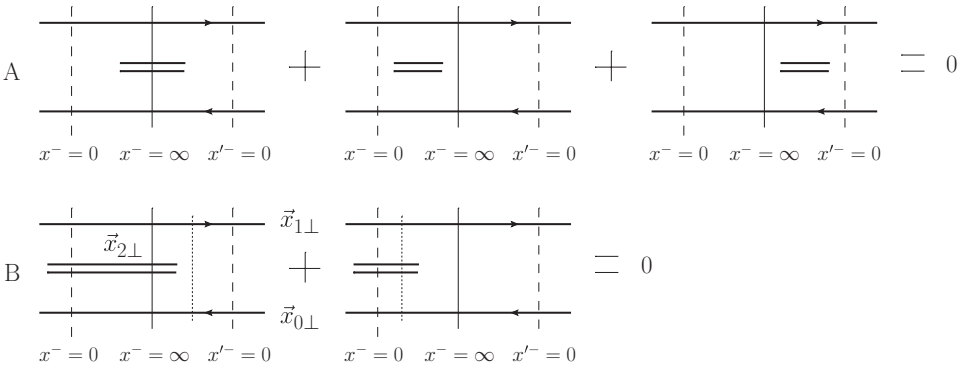

Fig. 7.10. Classes of diagrams with final-state interactions that cancel. The dotted vertical lines denote the intermediate states discussed in the text.

the logic of the lower panel in Fig. 7.8 and would include many more diagrams than the forward scattering amplitude in the upper panel of the same figure. Yet the answer for the total cross section should be the same regardless of the calculational strategy. One would like to see explicitly how a summation over all possible emissions and absorptions in the lower panel of Fig. 7.8 (without any constraints on the final state such as rapidity gaps) would lead to the diagram in the upper panel of Fig. 7.8. Understanding this question would give us a new insight into how the optical theorem works.

The answer to this puzzle is that all the emissions and absorptions for times after the interaction with the target, $x^- > 0$ and $x'^- > 0$, simply cancel. This cancellation of the final-state interactions was first proven by Chen and Mueller (1995) using a diagrammatic approach. We present the canceling diagrams in the large-N_c language of the dipole model in Fig. 7.10 using the notation introduced in Figs. 4.18 and 4.20. The cancellations are of two types. Type-A cancellations, shown in the first line of Fig. 7.10, involve a gluon that is emitted and absorbed in the final state, i.e., at $x^- > 0$, $x'^- > 0$. Type-B cancellations, shown in the second line of Fig. 7.10, involve a gluon that is emitted at $x^- < 0$ but is absorbed either at $x^- > 0$ or at $x'^- > 0$. (Cancellations in diagrams that are the complex conjugates of those of type B take place as well but are not shown, for brevity.)

The proof of the cancellations in Fig. 7.10 can be performed diagrammatically, following the original derivation of Chen and Mueller (1995). This is based on the fact that, for instance, the only difference between the two diagrams of type B is the sign of the LCPT energy denominators of the intermediate states denoted by the dotted vertical lines. When constructing an energy denominator the rules of LCPT require us to subtract the energy of the incoming state. However, since the energy of the whole process is conserved, the energy of the incoming state is equal to the energy of the outgoing state and we can equally well subtract the latter from the energy denominators. Since for $x^- > 0$ the energy of the target does not change any more, as the interactions with the target are over, we only need to consider the s-channel gluons. The intermediate state in the diagram on the left in row B in Fig. 7.10 then brings in a denominator with the energies of the quark and antiquark

https://doi.org/10.1017/9781009291446.008 Published online by Cambridge University Press

minus the energy of the same $q\bar{q}$ pair and a gluon in the final state. Since in the LLA the energies of the quark and antiquark change little, we get

$$\frac{1}{p_1^- + p_0^- - p_1^- + p_0^- - k_2^-} = -\frac{1}{k_2^-}, \tag{7.34}$$

where p_1^-, p_0^- are the quark energies while k_2^- is the gluon light cone energy. Similarly, the intermediate state denoted by the dotted line on the right in row B gives

$$\frac{1}{p_1^- + p_0^- + k_2^- - p_1^- + p_0^-} = \frac{1}{k_2^-}, \tag{7.35}$$

exactly equal to Eq. (7.34) in magnitude but opposite in sign. Since, as we have already mentioned, the remainders of the type-B diagrams are identical, we obtain the cancellation illustrated in Fig. 7.10B.

Similar sign changes in the energy denominators apply in the type-A case along with symmetry factors; the result is that the second and the third graphs are equal to minus one-half the first graph. (Note that a complete analysis of the diagrams of type A should include instantaneous terms like those shown in Fig. 4.14.)

One may also use the language of Chapter 5 to argue for the cancellation. Define the fundamental Wilson line over an arbitrary interval $[x_1^-, x_2^-]$ along the x^--axis (see Eq. (5.78)) by

$$V_{\vec{y}_\perp}[x_2^-, x_1^-] = \mathrm{P}\exp\left\{\frac{ig}{2}\int_{x_1^-}^{x_2^-} dx^- t^a A^{a+}(x^+ = 0, x^-, \vec{y}_\perp)\right\} \tag{7.36}$$

where the gluon field A^+ is either the classical field of the target or an effective field taking into account the small-x evolution corrections. The contribution of the final-state part ($x^- \in [0, +\infty]$) of a dipole–nucleus scattering diagram is then given by

$$V_{\vec{x}_{1\perp}}[+\infty, 0] \otimes V^\dagger_{\vec{x}_{0\perp}}[+\infty, 0], \tag{7.37}$$

where, as usual, the quark is at $\vec{x}_{1\perp}$ and the antiquark is at $\vec{x}_{0\perp}$, as shown in Fig. 7.10B. Squaring the amplitude we get

$$V_{\vec{x}_{1\perp}}[+\infty, 0]V^\dagger_{\vec{x}_{1\perp}}[+\infty, 0] \otimes V^\dagger_{\vec{x}_{0\perp}}[+\infty, 0]V_{\vec{x}_{0\perp}}[+\infty, 0] = \mathbf{1} \otimes \mathbf{1}. \tag{7.38}$$

All the interactions cancel and we end up with a noninteraction unit contribution. This cancellation is akin to the unitarity argument presented in Sec. 2.4.2, which was also used for construction of the dipole wave function in Sec. 4.3.

The cancellation of interactions at $x^- > 0, x'^- > 0$ and the identification of the $x'^- < 0$ part of the diagram in the lower panel of Fig. 7.8 with the $x^- > 0$ part of the upper panel reduces the amplitude squared to twice the imaginary part of the forward amplitude (according to the Cutkosky rules), in agreement with the optical theorem.

We are now ready to construct an evolution equation for the diffractive cross section $N^D(\vec{x}_{1\perp}, \vec{x}_{0\perp}, Y, Y_0)$. As we have seen before, with regard to the derivation of BK evolution, it is a little easier to construct the equation for the S-matrix than for the T-matrix. The

https://doi.org/10.1017/9781009291446.008 Published online by Cambridge University Press

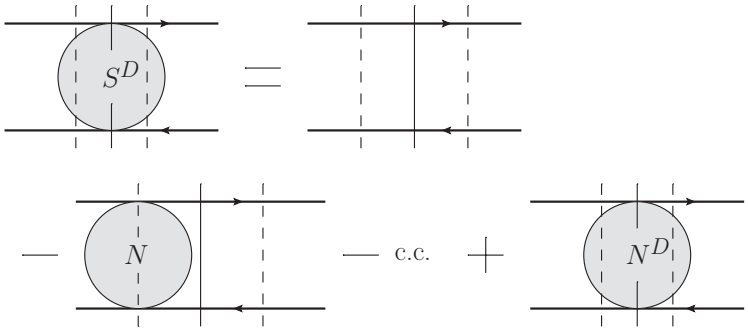

Fig. 7.11. Diagrammatic representation of the definition of S^D in Eq. (7.39). Here the dashed lines simply denote the times $x^- = 0$ or $x'^- = 0$. Interactions with the target are included only when these lines cross the shaded circles.

cross section N^D by definition contains the interaction with the target both in the amplitude and in the complex conjugate amplitude. We can complete it to an S-matrix-like object S^D by adding terms where there is no interaction either in the amplitude or in the complex conjugate amplitude (which gives $-N(\vec{x}_{1\perp}, \vec{x}_{0\perp}, Y)$ for each) and also terms where there is no interaction on either side of the cut (which gives 1). We thus define

$$S^D(\vec{x}_{1\perp}, \vec{x}_{0\perp}, Y, Y_0) = 1 - 2N(\vec{x}_{1\perp}, \vec{x}_{0\perp}, Y) + N^D(\vec{x}_{1\perp}, \vec{x}_{0\perp}, Y, Y_0). \tag{7.39}$$

The quantity S^D includes both the interacting and the noninteracting contributions to the left and to the right of the cut with the constraint that in the final state there is always a rapidity gap greater than or equal to Y_0. The definition (7.39) of S^D is illustrated in Fig. 7.11.

When $Y = Y_0$, using Eq. (7.33) we have

$$S^D(\vec{x}_{1\perp}, \vec{x}_{0\perp}, Y = Y_0, Y_0) = S^2(\vec{x}_{1\perp}, \vec{x}_{0\perp}, Y_0) \tag{7.40}$$

with S given by the BK/JIMWLK equations. We now want to derive the Y evolution for S^D for $Y > Y_0$, with the initial condition at $Y = Y_0$ given by Eq. (7.40). Suppose that in one step of the evolution we emit a gluon with rapidity $y > Y_0$. Since there are no final-state restrictions on gluons with $y > Y_0$ the gluon may or may not cross the cut and be present in the final state. (The rapidity gap is greater than or equal to Y_0; if the $y > Y_0$ gluon is not present in the final state this would simply extend the gap to rapidity y, which is still included in the definition of S^D.) A gluon with $y > Y_0$ may be emitted and absorbed at $x^- \lesseqgtr 0$ and $x'^- \lesseqgtr 0$. However, owing to the cancellations in Fig. 7.10, all emissions or absorptions at $x^- > 0, x'^- > 0$ cancel out, and we are left with the normal dipole evolution of the forward amplitude that we used in deriving the BK evolution equation, with all the emissions and absorptions taking place at $x^- < 0, x'^- < 0$. We conclude that the evolution for S^D is equivalent to that of the S-matrix, which in the large-N_c limit is given by Eq. (4.137) and

https://doi.org/10.1017/9781009291446.008 Published online by Cambridge University Press

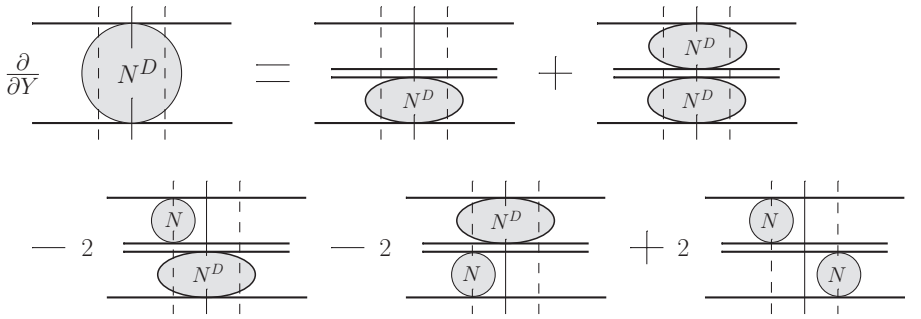

Fig. 7.12. A graphic form of the equation for the cross section of diffractive production. The dashed-line notation is the same as in Fig. 7.11.

illustrated in Fig. 4.26. Thus we can write

$$\partial_Y S^D(\vec{x}_{1\perp}, \vec{x}_{0\perp}, Y, Y_0) = \frac{\bar{\alpha}_s}{2\pi} \int d^2x_2 \frac{x_{10}^2}{x_{20}^2 x_{21}^2} \left[S^D(\vec{x}_{1\perp}, \vec{x}_{2\perp}, Y, Y_0) S^D(\vec{x}_{2\perp}, \vec{x}_{0\perp}, Y, Y_0) - S^D(\vec{x}_{1\perp}, \vec{x}_{0\perp}, Y, Y_0) \right]. \tag{7.41}$$

Substituting Eq. (7.39) into Eq. (7.41) we readily obtain (Kovchegov and Levin 2000)

$$\begin{aligned} \partial_Y N^D(\vec{x}_{1\perp}, \vec{x}_{0\perp}, Y, Y_0) &= \frac{\bar{\alpha}_s}{2\pi} \int d^2x_2 \frac{x_{10}^2}{x_{20}^2 x_{21}^2} \\ &\times \Big[N^D(\vec{x}_{1\perp}, \vec{x}_{2\perp}, Y, Y_0) + N^D(\vec{x}_{2\perp}, \vec{x}_{0\perp}, Y, Y_0) - N^D(\vec{x}_{1\perp}, \vec{x}_{0\perp}, Y, Y_0) \\ &+ N^D(\vec{x}_{1\perp}, \vec{x}_{2\perp}, Y, Y_0) N^D(\vec{x}_{2\perp}, \vec{x}_{0\perp}, Y, Y_0) \\ &- 2N(\vec{x}_{1\perp}, \vec{x}_{2\perp}, Y) N^D(\vec{x}_{2\perp}, \vec{x}_{0\perp}, Y, Y_0) \\ &- 2N^D(\vec{x}_{1\perp}, \vec{x}_{2\perp}, Y, Y_0) N(\vec{x}_{2\perp}, \vec{x}_{0\perp}, Y) + 2N(\vec{x}_{1\perp}, \vec{x}_{2\perp}, Y) N(\vec{x}_{2\perp}, \vec{x}_{0\perp}, Y) \Big]. \end{aligned} \tag{7.42}$$

This is a nonlinear evolution equation with the initial condition specified at $Y = Y_0$ in Eq. (7.33). To solve it one has first to solve the BK equation (4.138) to find the dipole amplitude N, which is then used in Eq. (7.42) to find N_D. Owing to the apparent complexity of both Eq. (7.42) and the BK equation, no analytic solution of Eq. (7.42) exists.

Equation (7.42) is illustrated diagrammatically (and, perhaps, somewhat schematically) in Fig. 7.12. We can see that in the nonlinear terms the factors 2 arise from adding diagrams that are mirror-reflected with respect to the cut diagrams shown. The coefficients in front of the nonlinear terms on the right-hand side of Eq. (7.42) turn out to be in agreement with the Abramovsky–Gribov–Kancheli (AGK) cutting rules (Abramovsky,

https://doi.org/10.1017/9781009291446.008 Published online by Cambridge University Press

Gribov, and Kancheli 1973), as was shown by Kovchegov and Levin (2000). The AGK cutting rules originate from the pomeron theory of high energy strong interactions but appear to work (almost always) in QCD in the LLA. The interested reader is referred to the original paper by Abramovsky, Gribov, and Kancheli (1973) and to a more recent paper by Bartels and Ryskin (1997).

A numerical solution of Eq. (7.42) was performed by Levin and Lublinsky (2001, 2002a). It was shown that the diffractive cross section resulting from Eq. (7.42) has a geometric scaling behavior and that the saturation scale for these processes has the same dependence on energy and atomic number A as the saturation scale for the total cross section. It was also predicted that the ratio $\sigma_{diff}/\sigma_{tot}$ has only a mild energy dependence and M_X^2-dependence, in agreement with an estimate from Eqs. (7.23) and, more importantly, with the HERA data (see Abramowicz and Dainton (1996), H1 collaboration (1997), and ZEUS collaboration (1999)).

Further reading

For further reading on diffraction we recommend the books by Barone and Predazzi (2002), Donnachie, Dosch, and Landshoff (2005), and Forshaw and Ross (1997). In these books a wide spectrum of different problems is discussed, from the wave nature of diffractive scattering to the practical phenomenology based on the reggeon approach. Several reviews of diffraction in DIS cover the topics that have been discussed here in more detail: Wusthoff and Martin (1999) (perturbative QCD), Hebecker (2000) (perturbative QCD and beyond, including the semiclassical approach to diffraction), and Weigert (2005) (the CGC approach to diffractive processes). We also recommend the review by Boreskov, Kaidalov, and Kancheli (2006), which gives an outline of diffractive processes using pomeron phenomenology, as well as the paper by Bartels and Kowalski (2001), where the space–time picture of diffractive processes is explored.

Low-mass diffraction with the production of a $q\bar{q}$-pair and a $q\bar{q}G$ state was discussed originally by Buchmuller, Gehrmann, and Hebecker (1997), Buchmuller, McDermott, and Hebecker (1999), and Kovchegov and McLerran (1999). We also recommend the papers by Munier and Shoshi (2004), Marquet (2005), and Golec-Biernat and Marquet (2005), Kopeliovich, Potashnikova, and Schmidt (2007), and Golec-Biernat and Luszczak (2009). In them one can find comparisons of the theory with the experimental data on diffraction.

For exclusive vector meson production in DIS we recommend the papers by Ryskin (1993) and Brodsky *et al.* (1994), along with the more recent paper of Marquet, Peschanski, and Soyez (2007).

As we have shown, high-mass diffraction is intimately related to the BFKL pomeron interaction, and the calculation of this process has been a main subject of interest in the community over several decades, starting from the Gribov, Levin, and Ryskin (1983) paper (see also Levin and Wusthoff (1994)).

High-mass diffraction in perturbative QCD was studied in the following papers: Levin and Wusthoff (1994), Bartels and Wusthoff (1995), Braun and Vacca (1997), Bartels, Braun, and Vacca (2005), and Bartels and Kutak (2008). Using a dipole approach, high-mass

https://doi.org/10.1017/9781009291446.008 Published online by Cambridge University Press

diffraction has been considered in papers by Bialas, Navelet, and Peschanski (1998, 1999), Korchemsky (1999), and Navelet and Peschanski (2001). Equation (7.42) has been rederived using methods different from those of Kovchegov and Levin (2000) in the following papers: Kovner and Wiedemann (2001) (using the eikonal approach), Hentschinski, Weigert, and Schafer (2006) (in the JIMWLK approach, generalizing Eq. (7.42) beyond the large-N_c limit), Kovner, Lublinsky, and Weigert (2006), and Hatta *et al.* (2006) (using general CGC concepts).

Exercises

7.1 Pick any diagram with a specific quark–gluon couplings in the type-B class from Fig. 7.10 and show explicitly that the cancellation does happen, as shown in the figure.

7.2 **(a)** Solve the following zero-transverse-dimensional equation for $S^D(Y, Y_0)$:

$$\partial_Y S^D(Y, Y_0) = \alpha_s [S^D(Y, Y_0)]^2 - \alpha_s S^D(Y, Y_0) \tag{7.43}$$

with the initial condition $S^D(Y = Y_0, Y_0) = [1 - N(Y_0)]^2$ (see Eq. (7.40)) with $N(Y)$ as found in Exercise 4.5(b).

(b) Using the result of part (a) find the diffractive cross section

$$M_X^2 \frac{d\sigma_{diff}}{dM_X^2} = -\frac{\partial N^D(Y, Y_0)}{\partial Y_0} = -\frac{\partial S^D(Y, Y_0)}{\partial Y_0}. \tag{7.44}$$

Plot it as a function of Y_0. You should get a function of Y_0 that peaks at a large Y_0 value that is close to Y: this maximum in the diffractive cross section is a direct manifestation of the saturation/CGC dynamics.

https://doi.org/10.1017/9781009291446.008 Published online by Cambridge University Press